Applied Catalysis B: Environmental 241 (2019) 471–482

Contents lists available at ScienceDirect

Applied Catalysis B: Environmental

journal homepage: www.elsevier.com/locate/apcatb

Modifying catalytically the soot morphology and nanostructure in diesel exhaust: Influence of silver De-NOx catalyst (Ag/Al_2O_3)

N. Serhan[a], A. Tsolakis[a,*], A. Wahbi[a], F.J. Martos[b], S. Golunski[c]

[a] Mechanical Engineering, University of Birmingham, Birmingham B15 2TT, UK
[b] Escuela de Ingenierías Industriales, University of Málaga, 29071 Málaga, Spain
[c] Cardiff Catalysis Institute, School of Chemistry, Cardiff University, Cardiff CF10 3AT, UK

ARTICLE INFO

Keywords:
Ag/Al_2O_3 catalyst
Soot morphology
Emissions
Hydrogen
GDI engine

ABSTRACT

The influence of an Ag/Al_2O_3 HC-SCR catalyst on the morphological and nanostructural aspects of the exhaust particulate matter (PM) generated during the combustion of diesel fuel and a glycol ether–diesel fuel blend was addressed in this research work. In addition, the impact of in-cylinder fuel post injections (FPI) on the particulate formation pathway and on the catalytic de-NOx efficiency was also studied.

The tests were carried at low exhaust temperatures in the absence and presence of small amounts of hydrogen (H_2). It is concluded that in the absence of H_2, the catalyst does not modify the primary particle size (dp_0) of the soot aggregates, while the aggregation of the soot particles throughout the catalyst channels is the main governing mechanism. The catalyst influence on the particulate structure was evident when H_2 was introduced, with smaller dp_0 seen downstream of the catalyst, indicating that despite the short residence time of the PM within the catalyst bed, the soot particles were partially oxidised. The use of late FPI reduces the exhaust PM level and delivers sufficient HC:NOx ratios that improves the catalyst activity up to a maximum of 80% NOx conversion, with no sign of catalyst deactivation when H_2 (500 ppm) was injected. Furthermore, it is suggested that along with oxidising part of the particles produced during the main fuel injection phase, late FPI can also produce, to a lesser extent, some additional soot with a less matured structure, resulting on average in less ordered particles being emitted into the exhaust stream.

This work shows that in modern diesel engines, a silver catalyst can alter the soot structure in the exhaust in a way that can ease the diesel particulate filter (DPF) regeneration cycles, improve its filtration efficiency and help in effectively reducing the tailpipe NOx emissions. For the catalyst to perform these functions, multiple in-cylinder fuel injection strategies (late FPI) combined with small amounts of hydrogen addition to the exhaust are required.

1. Introduction

Catalysts based on silver on alumina (Ag/Al_2O_3) can be designed to effectively combine both, diesel particulate matter (PM) oxidation [1–5] and selective catalytic reduction of nitrogen oxides (NO_x) with hydrocarbons (HC-SCR) at typical diesel engine exhaust gas temperatures (150–600 °C) [6–12].

Ag/Al_2O_3 offers high selectivity to nitrogen (N_2), low activity for sulphur dioxide (SO_2) oxidation along with high NOx conversion efficiencies (> 80%) at temperatures higher than 350 °C [7,12], but are also prone to deactivation by sintering [1]. Modern diesel engine exhaust temperature is low, often below 300 °C, thus the poor de-NOx activity is the main drawback for this technology. This is mainly attributed to the formation of stable surface nitrates through the reaction of the silver particles with nitrogen dioxides (NO_2) [2] along with the transformation of the gas-phase HCs into carbon-rich species that block the catalyst active sites (i.e. coking) [12–14].

Hydrogen (H_2) addition was reported as a key solution to increase the NOx conversion at low exhaust temperatures when enough reductants are available. The detailed mechanism by which H_2 enhances the de-NOx process has been widely investigated in the literature and the different proposed concepts can be found in several previous publications [14–16]. Furthermore, it was reported that H_2 addition can effectively oxidise the carbon-rich species trapped within the catalyst even in low temperature regions (185–300 °C) by favouring the oxidation of nitrogen oxides (NO) into NO_2 [13,14]. This kind of mechanism (oxidation) is expected to significantly modify the exhaust PM characteristics; however, no study to date has shown the impact on the

* Corresponding author.
E-mail address: a.tsolakis@bham.ac.uk (A. Tsolakis).

https://doi.org/10.1016/j.apcatb.2018.09.068
Received 10 July 2018; Received in revised form 14 September 2018; Accepted 19 September 2018
Available online 22 September 2018

morphological and nanostructural parameters of the PM. Identifying these variables is likewise necessary to decide if any modifications should be made to the current diesel particulate filter (DPF) design when HC-SCR is incorporated into an aftertreatment system.

Recent studies have shown catalyst activity improvements through optimising the exhaust HC:NOx ratio via fuel injections in the exhaust stream for the different engine conditions (i.e. exhaust temperature and space velocity) and by utilising range of HCs (light, heavy and oxygenated) as reductants [12,17,18]. Modern cleaner engines and improved quality fuels provide an opportunity for these catalysts to operate more effectively in reducing emissions [19]. Oxygenated diesel fuel combustion is reported widely to reduce the PM levels in the exhaust [20] and provide more reactive HCs species [17,21], parameters which are critical for the silver catalyst activity in reducing NOx emissions [19]. Furthermore, modern common rail fuel injection systems permit in-cylinder fuel post injection (FPI) strategies that can allow the optimisation of the unburned HCs quantity and quality in the exhaust [21–23]. Such injections were also reported to reduce the exhaust PM level, however to date, very little has been published [21] on the influence of late FPI on the particulate formation pathway and the resultant impact on the particulate structure.

Therefore, the main object of this study is to understand the level to which an Ag/Al_2O_3 HC-SCR catalyst can affect the morphological and nanostructural characteristics of the exhaust soot particles, in addition to De-NOx performance in the absence and presence of small amounts of H_2. The experimental studies have been conducted under a range of in-cylinder FPI strategies and fuelling types, including the use of diesel and tri-propylene glycol methyl ether (TPGME)/diesel blend (6.5 w.t.% oxygen content).

2. Experimental apparatus

In this study, a modern four-stroke single-cylinder, water cooled research diesel engine, equipped with a common-rail fuel injection system was used. The engine test rig consists of an electric dynamometer coupled into a load cell to load and motor the engine. Tests were carried out at a fixed speed of 1500 rpm under a constant engine load of 2 and 4 bar IMEP (Indicated mean effective pressure). The main engine specifications can be found in Table 1. The fuel was injected with a constant pressure of 600 bar and split between pilot (15 CAD BTDC), main (5 CAD BTDC) and different FPI timings (30 and 40 CAD ATDC for the 2-bar condition; 60, 70 and 80 CAD ATDC for the 4-bar condition). The pilot and FPI duration were maintained constant for 0.15 and 0.04 ms respectively, during all the tests. However, the corresponding main fuel injection duration was updated accordingly to generate the needed load condition. Upon introducing the FPI strategy, main injection was not modified and kept the same as in the passive mode (i.e. no FPI) to independently investigate the impact of the FPI application on the engine behaviour, emissions and particulates.

In-cylinder pressure was recorded over 200 cycles using an AVL GH13P pressure sensor mounted in the cylinder head and the signal was amplified by an AVL FlexiFEM 2P2 amplifier. The corresponding digital shaft encoder producing 360 pulses per revolution was used to measure the crank shaft position [21]. Heat release rate (HRR) was integrated from the pressure data collected by designing a simple model neglecting the heat loss differences between the fuels tested. The engine was warmed up prior to testing to minimize emission fluctuations associated with cold-start operation and ensure consistency of results.

The catalyst used was 2 mass % Ag/Al_2O_3 coated monolith catalyst supplied by Johnson Matthey Plc (Ø = 40 mm, L = 120 mm) with a high cell density of 600 cpsi. The catalyst was placed in a reactor inside a tubular furnace where K-type thermocouples (with a range of 0–1250 °C and an accuracy of ± 2.2 °C) were positioned upstream of the catalyst to ensure that the catalyst inlet temperature is maintained at the same level of the exhaust conditions.

The gas hourly space velocity (GHSV) was controlled and maintained constant at 35,000 h^{-1} by means of a suction pump located downstream the catalyst. Tests were conducted 10 min. after implementing each FPI strategy to ensure that the resulting emission levels had stabilised. H_2 was fed into the catalyst at flow rates that resulted in concentrations of 500, 1500 and 3000 ppm by volume. A one-way valve was used to negate the back-pressure effect and ensure the correct amount of H_2 was entering the catalyst. The engine was operated using an Ultra-Low Sulphur Diesel (ULSD) fuel supplied by Shell Global Solutions, and a TPGME/diesel blend (so called T20) containing 6.5 w.t.% oxygen content. The fuel specifications are extracted from the literature and detailed in Table 2.

The HC-SCR activity was monitored by measuring the exhaust gas emissions (NOx, NO, NO_2, CO and total HCs) upstream and downstream of the catalyst, using a MultiGas 2030 Fourier Transform Infrared Spectroscopy (FTIR). For adequate quantification of the different exhaust HCs species, the corresponding flame ionization detector (FID) response factors were sourced from the FTIR master file and implemented for each individual HC reading as follows: THC = (1.1 × methane) + (2.4 × acetylene) + (1.9 × ethylene) + (2 × ethane) + (2.85 × propylene) + (1.35 × FTIR-diesel (explained in Section 3.1)). Electrical mobility particle size distribution (d_{smps}) and the total particle number concentration were measured using a TSI scanning mobility particle sizer (SMPS) which includes a 3080-electrostatic classifier, 3081-Differential Mobility Analyser and a 3775-Condensation Particle Counter [31]. The exhaust dilution ratio was set to 1:11 using an ejector diluter system before testing the sample. PM was collected directly from the raw exhaust before and after the furnace assembly using copper grids with a coated Formvar/Carbon support film (200

Table 1
Engine specification.

Engine Parameters	Specifications
Engine type	Diesel 1-cylinder
Stroke type	Four-stroke
Cylinder bore × stroke (mm)	84 × 90
Connecting rod length (mm)	160
Compression ratio	16:01
Displacement (cc)	499
Engine speed range (rpm)	900–3000
IMEP range (bar)	< 7
Common Rail fuel pressure range (bar)	500-2000
Number of injections	3 injection events

Table 2
Fuel specification [24].

	Test method	ULSD	TPGME	T20
Chemical Formula	–	$C_{14}H_{26.1}$	$C_{10}H_{22}O_4$	–
FAME % (v/v)	**EN14078-A**	< 0.05	–	< 0.05
Viscosity (cSt T 40 c)	**D-445**	2.395	–	2.359
Lubricity, SLBOCLE, g	**D-5001**	3700	–	4100
Density (Kg/m^3) at 20 °C	**D-1298**	826.9	968 [25]	848.8
Latent Heat of vaporisation (kJ/kg)	–	243	330 [26]	357 [27]
Cetane number	**D-6890**	43.4 [28]	80 [29]	–
LCV (MJ/kg)	**D-3338**	43.11	28.1 [30]	39.55
Sulphur, mg/kg	**EN** 20884	< 10	–	< 10
Cloud point	**D-2500**	−21		−20
Flash point	**D-93**	71	> 110 [25]	76
Ash, mass %	**D-482**	< 0.01	–	< 0.01
10 % distillation (°C)	**D-86**	208.6	–	207.8
50% distillation (°C)	**D-86**	260.3	–	244.8
90 % distillation (°C)	**D-86**	319.2		308.5
wt.% C	**Calculated**	86.47	58.22	80.55
wt.% H	**Calculated**	13.53	10.75	12.95
wt.% O	**Calculated**	0	31.03	6.5
Oxygenates vol. (%)	**Calculated**	–	–	20.95

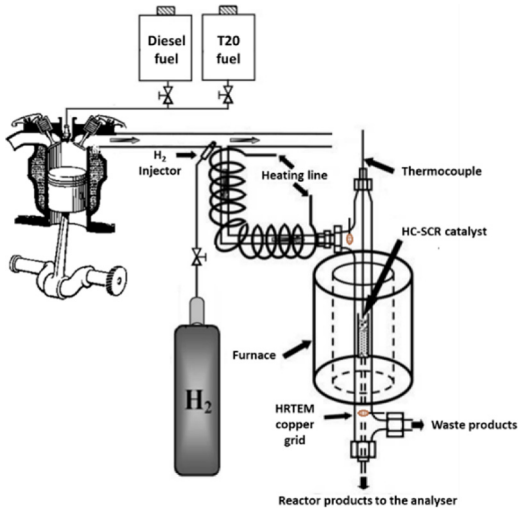

Fig. 1. Simplified schematic of the experimental setup.

mesh, 3.05 mm diameter, supplied from TAAB laboratories Equipment Ltd). The FEI Talos™ F200X S/TEM was used for the morphological (Radius of gyration, R_g; number of primary particles, np_0; and fractal dimension, D_f) and nanostructural (Fringes length, L_a; Fringes separation distance, d_{002} and fringes tortuosity, T_f) analyses of the sampled PM. The images were processed using digital image software built in MATLAB, following the method proposed by Lapuerta et al. [32,33] and Yehliu et al. [34]. The primary particle size distribution (dp_0) was also calculated using around 20 different TEM images for each condition (around 200 particles in total) and plotted as a normal-log distribution for each fuel and condition. A schematic diagram of the setup and the copper grid positions is shown in Fig. 1.

3. Results and discussions

3.1. Combustion behaviour and gaseous emissions

Neither fuel oxygenation nor the FPI strategies significantly affected the in-cylinder pressure nor the main-HRR peaks for both engine-operating conditions (Fig. 2). It is believed that this consistency resulted from the application of the pilot fuel injection, which is basically applied to thermally condition the cylinder for the main injection event. Such kind of injections lowers the impact of the fuel chemical properties and limits the influence of the FPI strategies [21]. However, as shown in Fig. 2, additional post-HRR curves were recorded at late positions of the expansion stroke with the application of the FPI, which can be described as a progressive combustion for the low load condition and instantaneous for the higher load test (more retarded FPI). This also explains the slightly higher exhaust temperatures recorded with this application (Table 3). Delaying the FPI slightly reduced the post-HRR peak level, therefore, the post-injected fuel is likely to be less efficiently combusted. This was expected since no sufficient temperature and pressure conditions are presented at the late stages of the expansion stroke to initiate the combustion reactions. In addition, late fuel injections indicate that there is shorter time for the combustion reactions to occur before the opening of the exhaust valve. As a result, when further delaying the FPI timing, less fuel is expected to participate in the combustion process, resulting in lower exhaust temperatures and in-cylinder pressure (compared to earlier injections) along with higher unburnt fuel portion (FTIR-Diesel and FTIR-T20 in Fig. 3) [35]. This also confirms that the FPI position is critical for the optimisation of the HC:NOx ratios (1:1–4.5:1) required for the HC-SCR reactions (Table 4). Concerning the break specific fuel consumption (BSFC), limited penalty of 0.35% and 0.23% was seen for the low-load and medium load testing respectively.

For the low-load condition, the light HC species (ethane, methane, and acetylene) remained below 8 ppm, and their concentrations were independent of the FPI timings for both fuels. Conversely, ethylene, propylene and formaldehyde steadily increased as the FPI timing delayed from 30 to 40 CAD ATDC, but their concentrations were still limited and did not exceed 27 ppm. With regards to the medium load condition, a higher proportion of light HCs was seen compared to the low load condition, indicating that even at these late FPI timings (60, 70 and 80 CAD ATDC), the post injected fuel is still undergoing combustion reactions [23]. However, retarding the FPI decreased the light HCs concentrations, indicating a poorer oxidation of the post injected fuel, as discussed earlier. Moreover, FPI strategies decreased the NO emissions while there was a simultaneous increase in the NO_2 levels, resulting in an overall NOx reduction. This trend could possibly result from the oxidation of NO into NO_2 by the hydroperoxyl radical (HO_2) resulting from the FPI application, along with the direct reaction of NOx with part of the higher hydrocarbons present in the exhaust [21]. A remarkable increase was seen in the CO emissions. FPI was applied at a late stage of the expansion stroke, in fuel rich regions, where the post-injected fuel could be partially oxidised instead of being completely

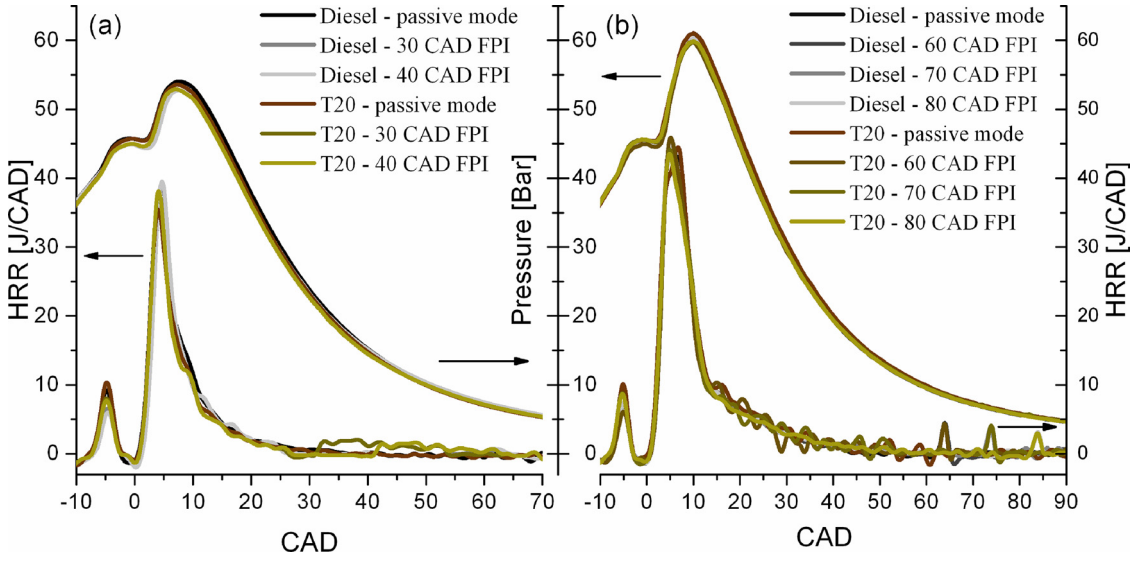

Fig. 2. In-cylinder pressure and its corresponding HRR curves for the different conditions tested.

Table 3
BSFC and exhaust temperatures under all test conditions.

Fuel	Load	Injection	BSFC (kg/kWh)	Exhaust temperatures (°C)	Fuel	Load	Injection	BSFC (kg/kWh)	Exhaust temperatures (°C)
Diesel	2 Bar	No post	0.3471	175	**T20**	2bar	No post	0.3572	173
	2.14	30 CAD	0.3483	186		2.13	30 CAD	0.3584	184
	2.11	40 CAD	0.3483	183		2.11	40 CAD	0.3584	182
Diesel	4 Bar	No post	0.4082	280	**T20**	4 Bar	No post	0.4201	278
	4.08	60 CAD	0.4091	293		4.07	60 CAD	0.4211	291
	4.03	70 CAD	0.4091	289		4.03	70 CAD	0.4211	287
	4.03	80 CAD	0.4091	284		4.02	80 CAD	0.4211	281

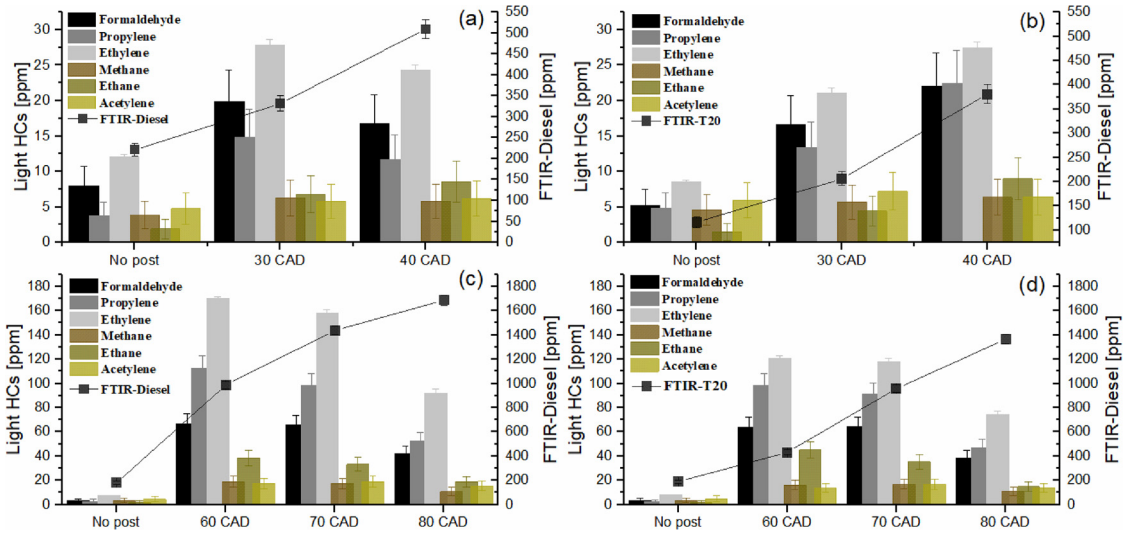

Fig. 3. HC speciation for different load combustions with different FPI timings for (a) diesel/2 bar, (b) T20/2 bar, (c) diesel/4 bar and (d) T20/4 bar.

Table 4
Emissions for the different HC:NOx ratios.

Fuel	Load	FPI	CO (ppm)	THC (ppm)	NO (ppm)	NO_2 (ppm)	NOx (ppm)	HC:NOx
Diesel	**2 Bar**	No post	306 ± 7.49	253 ± 15.9	171 ± 7.96	49 ± 7.07	220 ± 8.65	1.15
		30 CAD	403 ± 10.07	380 ± 19.49	143 ± 8.32	57 ± 6.45	200 ± 10.96	1.90
		40 CAD	406 ± 8.14	560 ± 23.66	138 ± 7,95	62 ± 4.32	200 ± 9.21	2.80
T20	**2 Bar**	No post	236 ± 15.36	150 ± 12.24	160 ± 9.63	52 ± 7.22	215 ± 15.42	0.69
		30 CAD	326 ± 12.05	280 ± 16.73	142 ± 6.8	56 ± 8.21	198 ± 8.85	1.41
		40 CAD	340 ± 11.43	500 ± 22.36	138 ± 8.64	58 ± 7.74	196 ± 10.45	2.55
Diesel	**4 Bar**	No post	200 ± 7.14	190 ± 14.14	434 ± 10.33	62 ± 7.87	530 ± 8.27	0.36
		60 CAD	490 ± 12.13	1042 ± 32.28	408 ± 8.23	72 ± 4.65	480 ± 6.68	2.17
		70 CAD	535 ± 13.13	1817 ± 42.62	410 ± 12.43	72 ± 6.32	482 ± 10.66	3.76
		80 CAD	390 ± 11.74	2050 ± 45.27	408 ± 10.21	73 ± 8.48	480 ± 9.54	4.27
T20	**4 Bar**	No post	158 ± 12.56	160 ± 14.07	450 ± 13.97	65 ± 8.08	515 ± 8.46	0.31
		60 CAD	450 ± 11.21	650 ± 25.49	398 ± 10.32	72 ± 8.57	470 ± 13.43	1.38
		70 CAD	500 ± 9.36	1292 ± 35.94	400 ± 9.43	72 ± 9.22	472 ± 8.44	2.73
		80 CAD	389 ± 13.72	1730 ± 41.59	396 ± 8.62	74 ± 8.6	470 ± 7.23	3.68

combusted, and as a result both CO and hydrogen (H_2) were produced according to Eq. (1):

$$C_xH_y + \frac{x}{2}O_2 \rightarrow xCO + \frac{y}{2}H_2 \quad (1)$$

Jeftic et al. [35] also suggested that with late fuel injections, the higher amounts of CO could even result from steam reforming of the HCs, as shown in Eq. (2):

$$C_xH_y + xH_2O \rightarrow xCO + \left(x + \frac{y}{2}\right)H_2 \quad (2)$$

Concerning the T20 fuelling, a slight increase in the engine BSFC was shown compared to diesel. This is mainly due to the lower energy density of T20 (Table 2) which indicates that a higher volumetric fuel consumption is required to counterbalance the energy loss and maintain similar load conditions [36,37]. Furthermore, the higher latent heat of vaporisation of the T20 blend (Table 2) reduced the maximum flame temperatures compared to that of the diesel combustion, and as a result decelerated the thermal NO formation mechanism (Table 4) and dropped the exhaust temperatures (Table 3) [38]. In addition, the oxygenated moieties present in T20 reduce the carbon mass fraction in the fuel blend (reducing the rate of CO formation [39]) and promote the HC oxidation (i.e. less light HCs and unburnt fuel) [36].

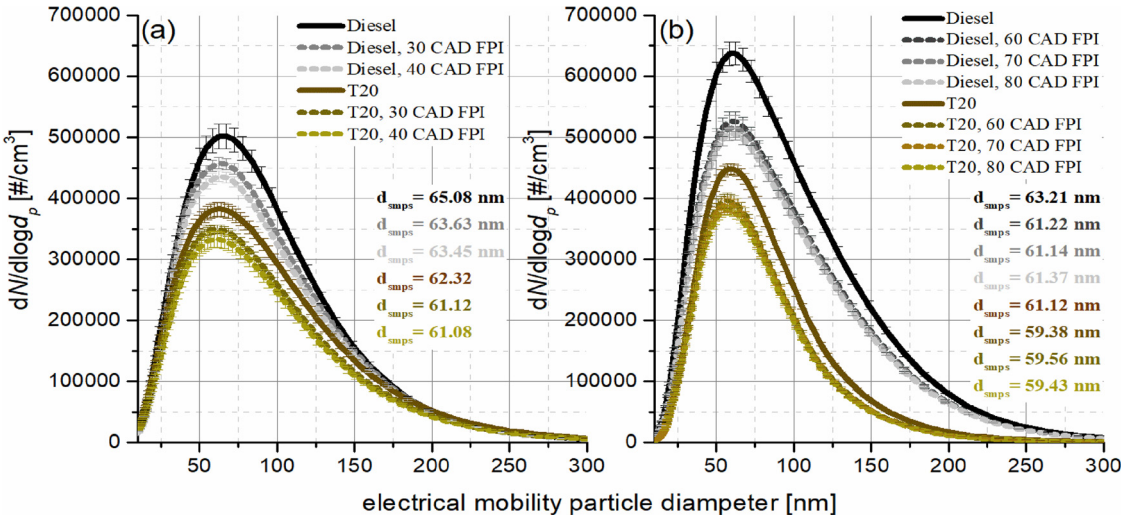

Fig. 4. Particle size distribution from the different fuelling and FPI strategies at (a) low load and (b) medium load conditions.

3.2. Particulate matter emissions

T20 fuelling resulted in a substantial reduction in the PM emissions along the whole distribution for both load conditions with/without the presence of the FPI. In addition, a small decrease in the average electrical mobility particle diameter (d_{smps}) was seen (Fig. 4). The effect of the T20 fuelling on the particles concentration level and physico-chemical properties was discussed in detail in our previous work [40].

Reagrding the FPI application, PM level and d_{smps} also presented a noticeable reduction for both fuels combustion and seems independent from the FPI timing.

To further assess these results, morphological and nanostructural analyses were carried out to understand the effect of these strategies on the soot formation pathway and oxidative reactivity (i.e. ability of the particles to oxidise). Following the similar effect of FPI for both load conditions (i.e. smaller d_{smps} and lower particles level), analysis was only carried out for the medium engine load test, including the particles collected from the passive (no FPI) and 80 CAD FPI use.

Interestingly, even though FPI was implemented very late in the cycle, remarkable changes were seen along all the particles morphological parameters. As shown in TEM analysis (Fig. 5a and b), particles with smaller radius of gyration (R_g) and fewer number of primary particles (n_{p0}) were produced with respect to the passive mode combustion, which in turn confirms the SMPS results shown earlier in Fig. 4. As for the particle shape (i.e. chain-like or spherical), it can be evaluated by referring to its fractal dimension (D_f), with higher values

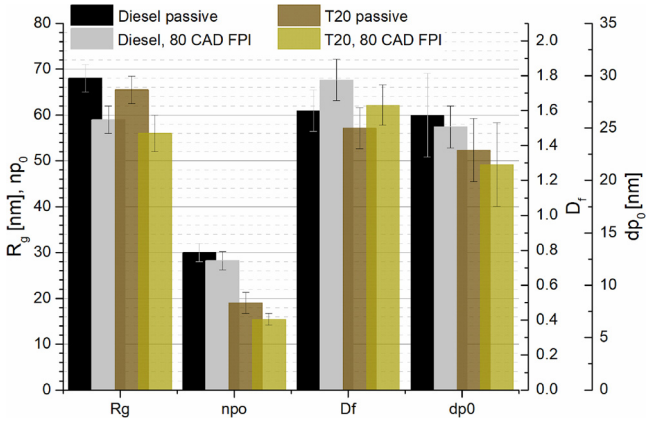

Fig. 5. (a) R_g, np_0, D_f, and (b) primary particle size distribution under the 4 bar IMEP load condition in passive and 80 CAD FPI mode.

indicating a more spherical profile [41]. The lower level of particulate emitted in the FPI case reduces the probability of collision between the particles, and as a result, more spherical aggregates were shown in the analysis (Fig. 5a). With regards to the average primary particle size (dp_0), only a slight reduction limited to 1.5% was detected, compared to the passive mode for both fuelling conditions.

Nevertheless, despite the fact that no statistically significant changes were seen along dp_0 (i.e. results still within the error bars), the structure and arrangement of the particulate carbon layers were notably modified. Shorter graphene lamelaes (L_{002}) characterised with a more curved silhouette (i.e. higher tortuosity (T_f)) were spotted within the particles produced from the FPI combustion, with no observable modifications seen in the layers separation distance (d_{002}). Such kind of alterations highlight the presence of more disordered particulates in case of FPI, which in turn indicates that the resulted soot is more vulnerable towards oxidation.

The influence of late FPI on the particulate formation pathway is under debate in the literature: Molina et al. [42] and Arregle et al. [43] developed the “split flame” theory which presumes that, regardless of the injection dwell, the main and post fuel (if later than 20 CAD) combustion are independent. Otherwise stated, the reduction along the PM level with FPI introduction results from the shortened main injection phase, while the late post fuel injected was suggested to be a soot-free combustion process. However, other authors [21,35] suggested that this reduction is mainly due to an enhancement in the oxidation of the particles produced during the main injection phase. This was expected to be the outcome of (a) an improvement in the late cycle air-fuel mixing, which help in introducing fresh oxygen to the mixture and thus reduce the local equivalence ratio, (b) increasing the in-cylinder temperature at the late stages of the expansion stroke (as shown from the post-HRR peaks in Fig. 2).

In this work, the reduction shown along the particle R_g and d_{smps} confirms that the particulate undergoes an improved oxidation process during the combustion phase, which suggests that the post injection flame does influence the main injection mixture.

Combustion temperature and soot residence time is widely accepted as the main factors governing the extent to which the particles will be graphitised during the combustion process. In general, increasing the soot residence time at elevated temperatures promotes the particulate carbonisation process and result in more ordered particles. Therefore, in the case where the combustion of the post-fuel will yield additional soot to the chamber, it is expected to be less mature (i.e. more reactive) than that produced from the main injection pulse. This is expected since at late stages of the expansion stroke, the in-cylinder temperature levels

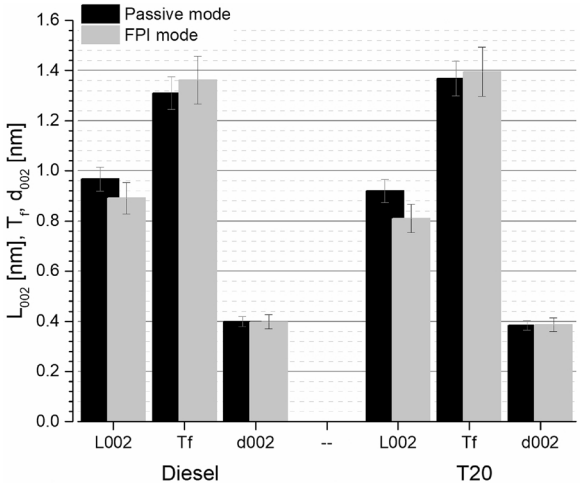

Fig. 6. Different nanostructural parameters resulting from the passive and FPI mode for both diesel and T20 combustion.

and the remaining residence time for the particles before the quenching of the combustion reactions is lower than that experienced by the particles produced near the top dead centre.

According to the modification shown along the particle nanostructure (Fig. 6), where on average, slightly more disordered particles were seen in case of the FPI combustion, it can be speculated that despite the late FPI timings, the fuel combustion at that stage is still producing some additional soot. However, following the reduction shown in the exhaust particles level (Fig. 5), it can be suggested that the proportion of soot (resulting from the main pulse) undergoing oxidation is significantly greater than that produced from the post fuel combustion.

3.3. Influence of the FPI on the HC-SCR activity

3.3.1. Passive mode (No FPI introduction)

Fig. 7 shows the variation in the initial (during 1st minute of the test) and steady state (after 15 min) de-NOx catalyst activity (NO, NO_2 and NOx) along with the HCs conversion efficiency when using different FPI strategies and 500 ppm H_2, at the 2-bar and 4-bar engine load conditions. In the passive mode, the de-NOx activity of the HC-SCR was very limited as only 22% (2 bar) and 34% (4-bar) NOx conversion was achieved with both fuelling. This was due to the low exhaust temperatures available (185–285 °C) which were not sufficient to activate the HCs into reactive intermediates (i.e. oxygenates).

The injection of small concentrations of hydrogen (500 ppm) into the exhaust feed drastically improved the de-NOx activity for both fuels in the initial stages of the reactions, with T20 showing remarkably higher conversion compared to diesel in the low load. However, the activity slowly deteriorated with time (15 min) before finally reaching 44% and 51% NOx conversions in the 2-bar and 4-bar mode respectively, with no noticeable difference between diesel and T20. Inspecting the residual HC concentrations downstream of the catalyst, it can be clearly seen that the loss in the de-NOx activity is not attributed to any type of catalyst deactivation but directly related to the lack of hydrocarbons available in the exhaust (HC conversion > 80%).

The increased activity seen in the presence of the H_2 is directly attributed to its role in activating (or lowering the activation energy) of the molecular oxygen (O_2) to produce reactive oxygen species such as HO_2 and O_2^- [44,45]. These species react readily with exhaust HCs, increase the rate of NOx absorption over the catalyst surface [14,15] and reduce the stability of the surface nitrate species that block the active Ag sites [15,46,47]. Further detail for the exact mechanism by which H_2 activates the Ag/Al_2O_3 surface can be found in a previous publication [16]. Furthermore, from the increased level of NO_2 (which gives rise to the apparent negative conversion) in the presence of H_2, we can speculate that in the absence of the needed HCs to initiate the SCR reactions, H_2 only activates the NO-NO_2 conversion pathway.

3.3.2. FPI mode

FPI strategy was implemented at 30 and 40 CAD (2-bar) and 60, 70 and 80 CAD ATDC (4-bar) to gradually increase the exhaust HC:NOx ratio for both fuelling conditions as detailed in Table 4. More retarded FPI for the medium load condition was required to compensate for the greater loss of HCs by oxidation at this relatively high in-cylinder temperature. Retarding the FPI timing improved the catalyst de-NOx activity for both fuelling conditions with minor differences seen between diesel and T20 combustion in the absence of H_2. In the 2-bar engine condition, the NOx conversion increased to 30% and 40% at 30 and 40 CAD FPI strategies respectively. In the 4-bar, better de-NOx activity was seen with a conversion of 40%, 48% and 50% for the 60, 70 and 80 CAD FPI respectively. It should be noted that the conversion efficiencies achieved in the low load test are considerably higher than that reported in our previous work (20%) [13], where diesel fuel was directly injected into the exhaust pipe to control the HC:NOx ratio. We suggest that the enhancement in the catalyst activity is due to hydrogen production by the FPI strategies as discussed earlier in Section 3.1.

With the injection of 500 ppm of H_2 in the 2-bar mode, NOx conversion significantly increased and stayed in the range of ~70% at both 30 and 40 CAD FPI, for both fuelling conditions. Furthermore, no significant changes were seen between the two FPI timings since 30 CAD FPI was sufficient to deliver the optimal HC:NOx ratio (~1:1) (Table 4) for this exhaust temperature condition, as shown in our previous work [13]. No signs of catalyst deactivation were observed during the test period (around 15 min for each condition). Conversely in the 4-bar mode, the 60 CAD FPI strategy failed to produce the required level of HCs to undergo the de-NOx reactions, while 70 and 80 CAD FPI resulted in sufficient reductants in both fuelling conditions. The maximum catalytic conversion was achieved at 80 CAD FPI reaching 68.75% and 79% for diesel and T20 combustion respectively.

It is important to note that despite the relatively lower HC:NOx ratios recorded under all the FPI timings with the T20 combustion, the catalyst was able to reach similar NOx conversion as in the diesel case at the 2-bar mode and better conversions were seen for the 4-bar mode. Along with the cleaner combustion (reduced PM level) recorded from the T20 fuelling, the reactivity of the oxygenated species (TPGME) strongly dictates the catalyst de-NOx activity [7]. Following the results of Shimizu et al. [48], the oxygenated hydrocarbons activity over an Ag/Al_2O_3 HC-SCR catalyst change in the following order: “ethers > alcohols > aldehyde > ester > ketone” in the absence of H_2 and “ethers > alcohols > ester > ketone > aldehyde” in the presence of H_2. No studies to date have identified the intermediates in glycol ethers-SCR reactions over Ag/Al_2O_3 coating, such as TPGME in our case. However, the molecular structure of this oxygenate incorporates both alcohol and ether functional groups, and as a result a considerably high reactivity is expected for the TPGME molecule. Furthermore, its shorter chain length and lower viscosity compared to the different HCs in the diesel fuel offer a better diffusivity to the catalyst surface which eases the access of the reductants to the catalytic active sites [19]. In addition, glycol ethers are polar in nature (contain OH group) and are miscible in water, which is also considered an advantage compared to the other HC species in diesel since they can compete successfully with water for adsorption sites on the catalyst [19]. The higher reactivity of the TPGME molecule is also confirmed in this work by the higher conversion rate of the unburned hydrocarbons in the case of T20 compared to diesel, especially in the low load case (Fig. 7). In the 4-bar mode, another possible reason for the better catalyst activity with T20 could be inferred from the fuel distillation curve. Following the work of Smith et al. [49], 45–55% and 65–70% of the HCs present in diesel and T20 fuel respectively are expected to be in the vapour phase when the exhaust temperature is in the range between 285 and 295 °C. It is

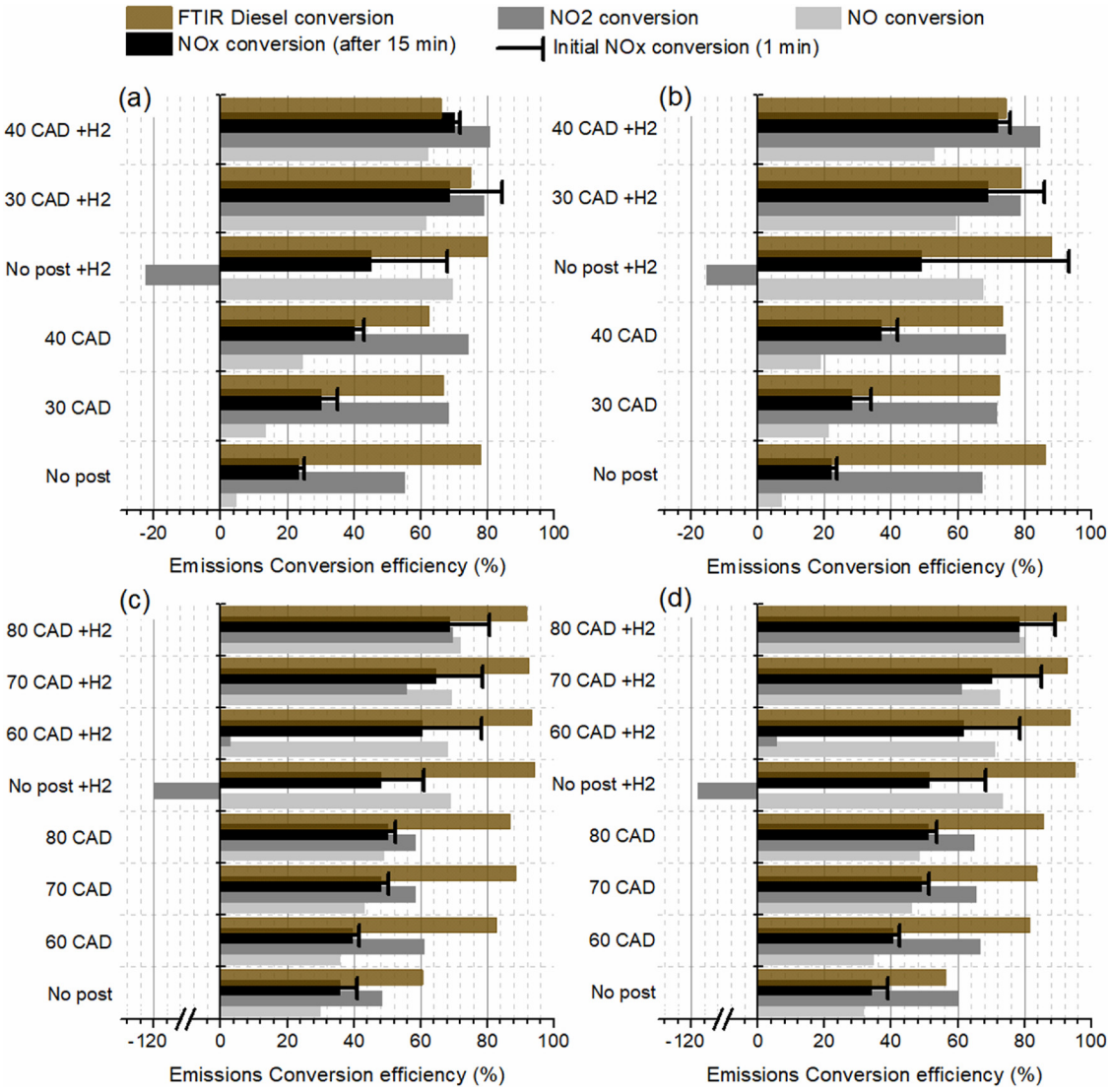

Fig. 7. Emissions conversion efficiency including NO, NO_2, NOx and THC within the HC-SCR for (a) diesel 2-bar, (b) T20 2-bar, (c) diesel 4-bar and (d) T20 4-bar.

therefore suggested that in the case of the T20 combustion, a greater portion of the reductants will undergo the de-NOx reactions in the gaseous state and thus better catalytic activity was seen compared to the diesel.

3.3.3. Catalyst De-NOx sensitivity to H_2 addition

To test the H_2 effect, higher amounts of 1500 ppm and 3000 ppm were introduced downstream the catalyst, but only the 40 CAD FPI (2-bar condition) and 80 CAD FPI (4-bar condition) events were tested since considerably higher amounts of HCs had survived the catalyst reactions compared to earlier injections (Fig. 7). Due to the similarity of the results between both fuelling, only the T20 case is considered below.

In the 2-bar condition, the addition of higher amounts of hydrogen had insignificant improvement on the activity of the catalsyt which could be due to the inability of the HCs to activate beyond this point at this low temperature condition (~185–190 °C). Furthermore, it should be noted that in the literature, most of the HC-SCR real engine testing incorporates old engine technologies as a source for the exhaust gas [12–14,17,50], where significantly higher PM level is expected compared to this work. Therefore, it can be speculated that in our study, the rate of soot deposition in the catalyst is considerably lower than that reported in the above references. As a result, additional amounts of H_2 were not necessary to help in oxidising the trapped particles, as it is advised in the literature [17].

As for the 4-bar condition, increasing the H_2 concentrations had adverse effects on the catalyst de-NOx activity, as during that process NOx concentrations downstream the catalyst sharply increased from 100 ppm to 170 ppm and 270 ppm once the H_2 concentration was increased from 500 ppm to 1500 ppm and 3000 ppm respectively (Fig. 8b). This indicates that at this temperature condition, H_2 introduction should be adequately optimised to avoid any unwanted oxidation of the HCs instead of their activation.

3.4. Particles morphology

Metal catalysts have the ability to trap and oxidise exhaust PM when enough soot residence time within the catalyst is provided (i.e. coated DPF) [1–5]. Coking mechanism was not evident during all the tests since no clear catalyst deactivation was recorded at all the exhaust temperature range (low and medium load testing). The absence of that mechanism (coking) highlights the possibility of an efficient oxidation of the particles throughout the catalyst despite the limited soot residence time provided in such kind of catalysts (flow-through substrate). Thus, to better understand the impact of the catalyst on the soot structure, the morphology and nanostructure of the particles collected

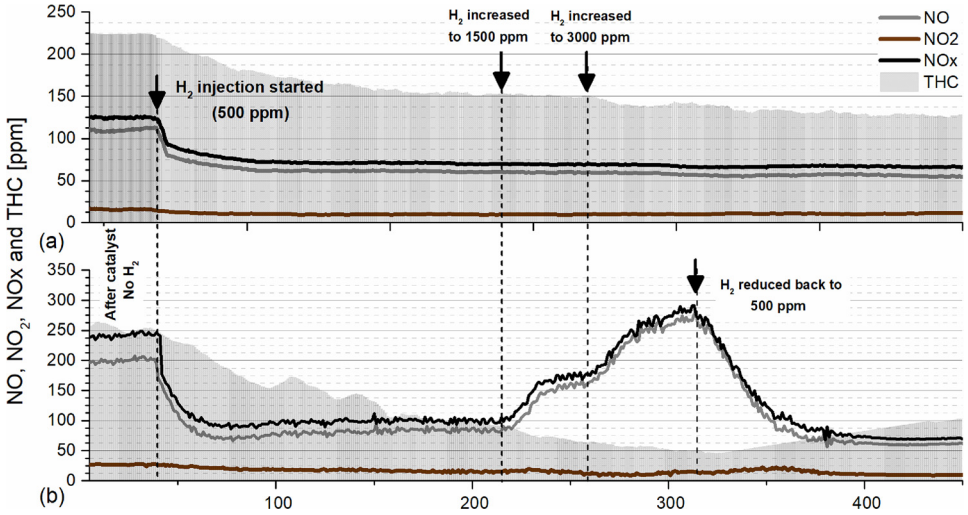

Fig. 8. Hydrogen effect with different load conditions: (a) 2-bar IMEP, (b) 4-bar IMEP.

upstream and downstream the catalyst with/without the presence of H_2 for the different fuelling and loading conditions was examined.

3.4.1. Catalyst effect at low load condition

It can be clearly seen from Fig. 9 that the average number of primary particles (np0) in the aggregates and their corresponding size (Rg), with or without the presence of H_2, significantly increase within the catalyst for both fuelling combustions. This trend presents a clear indication that just a limited fraction of the particles have been trapped within the catalyst, a hypothesis that has been proposed earlier by Fayad et al. [51]. It is concluded that the dominating mechanism at this testing condition is the aggregation of the inlet particles which is favoured by the enhanced collision between the particulates throughout the HC-SCR channels [51]. It should be noted that due to the localised thermal effect of the hydrogen gas and the hydrocarbon oxidation mechanism (exothermic), the internal and global catalyst temperature is likely to increase during the de-NOx process. This could explain the slightly higher D_f recorded downstream of the catalyst, since beside the enhanced aggregation mechanism, the temperature increase throughout the catalyst can thermally restructure the particles shape and make it more spherical. Even though the particles surviving the catalytic reactions show a more spherical shape (i.e. worsen the DPF filtration efficiency) [51], the significant increase in their R_g is considered as a beneficial parameter that can increase their trapping probability within the DPF.

Concerning the average primary particles size (dp_0), no statistically significant changes were seen in the absence of H_2 (Fig. 10). Interestingly, introducing H_2 reduces dp_0 by 2.7% and 3.6% for diesel and T20 fuelling conditions, indicating that the particles have been partially oxidised throughout the catalyst. The increased reduction in dp_0 seen in case of T20 is directly attributed to the enhanced oxidative potential of the particles resulting from T20 combustion compared to diesel as reported previously in Ref. [40].

NO_2 is known to be a stronger soot oxidant than O_2, since it can convert carbon to CO and CO_2 in the low-temperature range of 200–500 °C, through the reactions below [52]:

$$C(s) + NO_2 \rightarrow CO + NO \quad (3)$$

$$C(s) + 2\,NO_2 \rightarrow CO_2 + 2NO \quad (4)$$

Villani et al. [2], reported that nitrated Ag/Al_2O_3 is effective at lowering the onset temperature for carbon oxidation under typical diesel exhaust conditions. This was attributed to the formation of small metallic silver particles (Ag°) on the catalyst surface at a temperature of 400 °C, which help in oxidising NO into the needed NO_2 for the soot oxidation mechanism. However, in the presence of small amounts of H_2, Ag/Al_2O_3 can shift this mechanism (Ag° formation) to significantly lower exhaust temperatures (~200 °C), as demonstrated by Breen et al. [15] and Kim et al. [16]. This was also confirmed in this study, since in the presence of H_2, an increased level of NO_2 was detected downstream

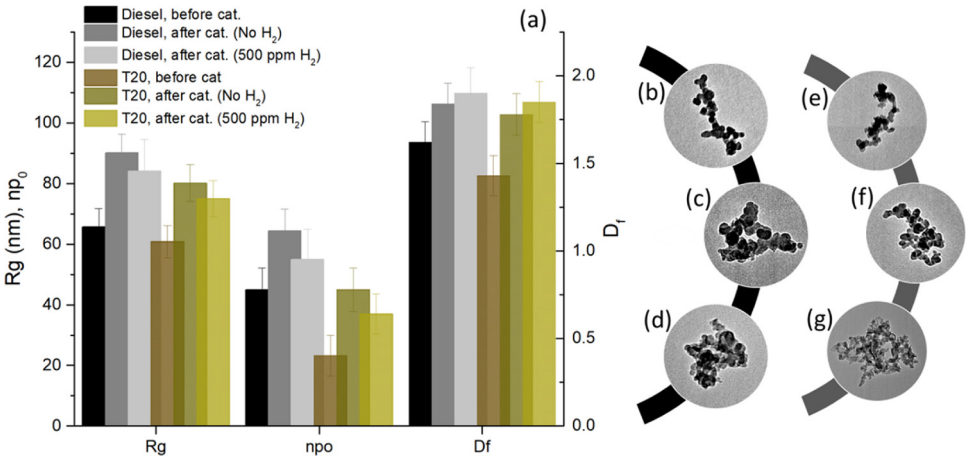

Fig. 9. (a) R_g, np_0 and D_f before and after the HC-SCR catalyst with/without H_2 addition at low load condition. (b, e) TEM micrograph for diesel and T20 particles before catalyst respectively, (c, f) after cat without H_2 addition, (d, g) after cat with H_2 addition.

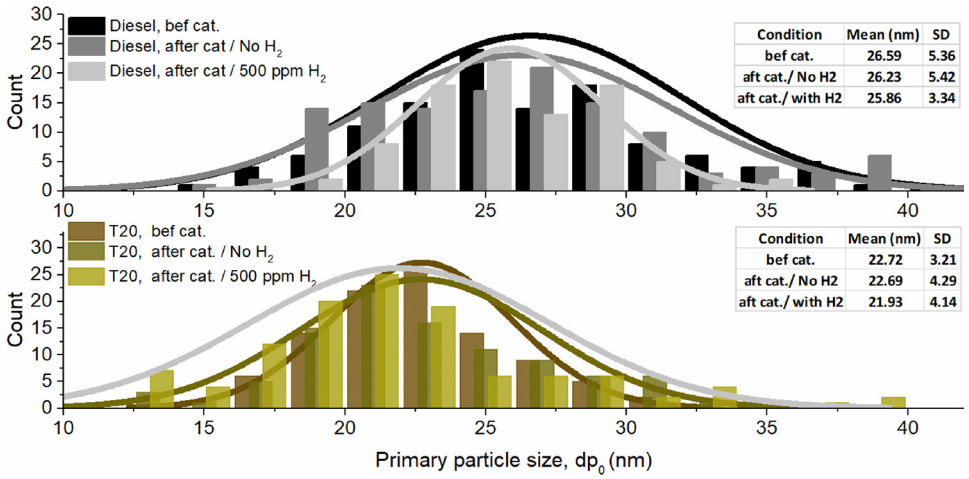

Fig. 10. Primary particle size distribution (dp_0) before and after the HC-SCR catalyst at low load condition for diesel and T20.

of the catalyst when insufficient reductants were available (Fig. 7). Also, H_2 addition over an Ag/Al_2O_3 surface promotes the formation of several highly active surface phases, such as AgO, Ag_2O_3 and $Ag(OH)_2$) [16] and can also promote the formation of superoxide O_2^- ions [53]; these species might assist the carbon oxidation by O_2 [5]. Thus, it can be speculated that despite the limited residence time of the soot within the catalyst, the higher NO_2 emissions and active oxygen species formed in the presence of H_2, are the governing factors in enhancing the oxidation of the exhaust particles.

3.4.2. Catalyst effect at medium load condition

In the absence of H_2, the same trend reported earlier in the low load testing was seen again under this condition, thus it will not be further discussed in this section. R_g, np_0 and D_f increased downstream of the catalyst (Fig. 11a), while dp_0 remained constant with minor reduction seen only in the T20 case (Fig. 12). However, when H_2 was introduced, the catalyst influence on the particulate morphology was more obvious, with significant changes being seen compared to the low load case. Concerning the diesel combustion, the aggregate np0 was reduced by 22% and dp0 by 5.29%, resulting in a total reduction of 10.16% along the particles Rg. Moreover, aggregates with more chain-like structure (lower Df) were detected downstream of the catalyst. These results confirm that, with a slightly higher exhaust temperature, which is still considered as a low temperature region, a small amount of H_2 addition was capable of effectively oxidising the exhaust particulate compared to the low load case. The higher exhaust temperatures recorded (around 295 °C) are sufficient to fully activate the NO_2-soot oxidation mechanism [52] and it is expected that under this thermal environment, the localized thermal effect of H_2 will also promote the direct soot oxidation by oxygen [54]. In addition, the more chain-shape morphology seen downstream of the catalyst indicates that along with easing the particles oxidation, HC-SCR can also enhance the DPF functionality (i.e higher trapping efficiency).

It should be noted that with regards to the T20 fuel combustion, no statistically significant number of soot aggregates were detected on the copper grids positioned after the catalyst. Most of the examined particles could be described as hydrocarbon droplets (mostly oxidised particles) as shown in Fig. 11g, and as a result this prevented us for producing a confident morphological/nanostructure analysis.

3.5. Particles nanostructure and oxidation

To further confirm the reduction shown along dp_0 (i.e. oxidation of particles) throughout the catalyst, a detailed nanostructural analysis was conducted to investigate the catalyst impact on the particulate carbon layer arrangement and structure. Following the inconspicuous changes shown along dp_0 in the absence of H_2, the analysis in this section will be only conducted on the soot particles collected in the presence of H_2. The different nanostructural results were presented in Fig. 13 as a ratio of the post-SCR values over the pre-SCR values to show in detail the variations between the different particles inspected.

It is seen that for the low load condition, the post-SCR particles (both diesel and T20) present significantly shorter carbon layers, characterised with higher tortuosity compared to the pre-SCR particles.

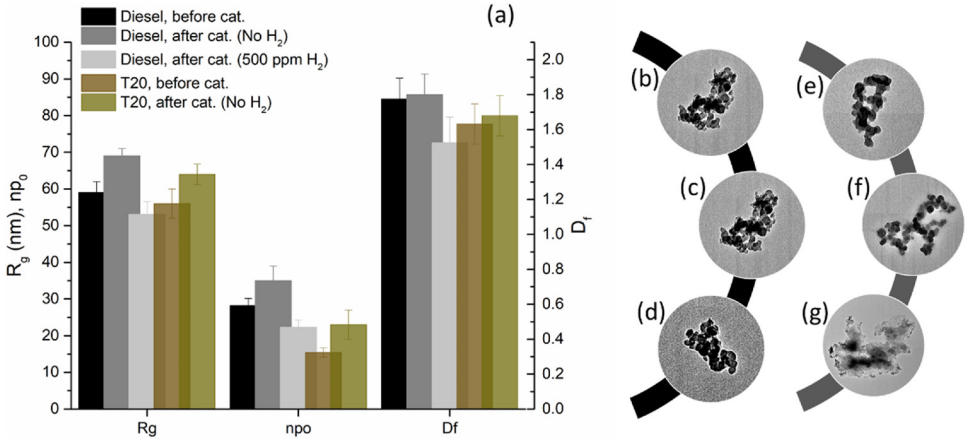

Fig. 11. (a) R_g, np_0 and D_f, before and after the HC-SCR catalyst with/without H_2 addition at medium load condition. (b, e) TEM micrograph for diesel and T20 particles before catalyst respectively, (c, f) after cat without H_2 addition, (d, g) after cat with H_2 addition.

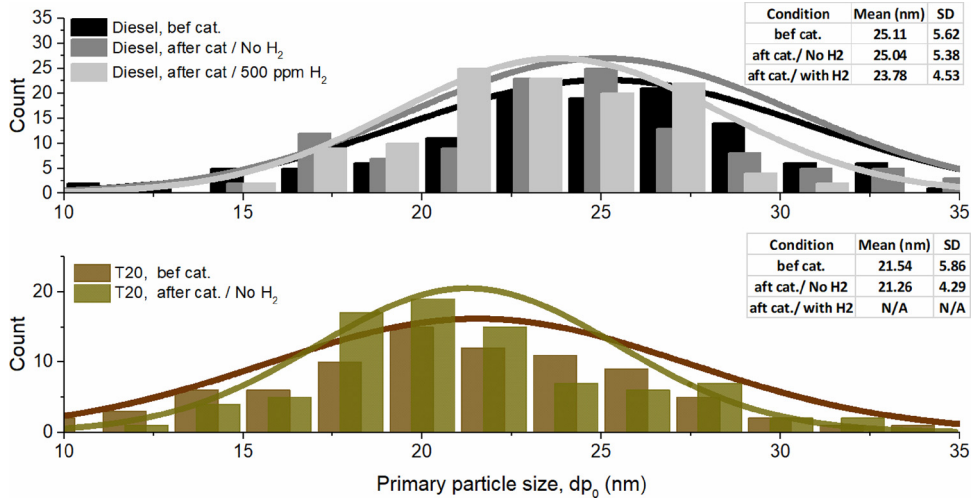

Fig. 12. Primary particle size distribution (dp_0) before and after the HC-SCR catalyst at medium load condition.

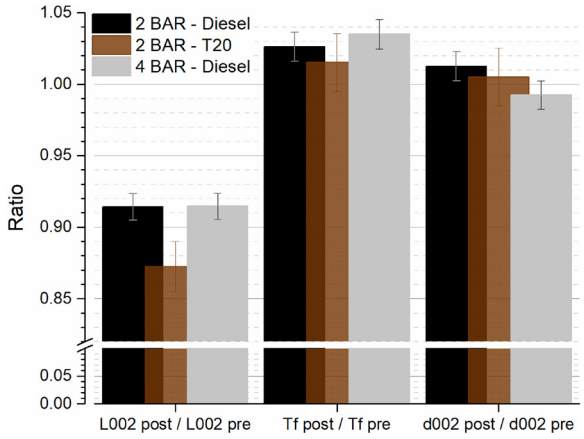

Fig. 13. Nanostructural parameters ratios including L_{002}, T_f and d_{002}.

As for d_{002}, minor variations ($d_{002\ post}$ / $d_{002\ pre}$ ~ 1) falling within the data error bars were observed. The better reactivity of the T20 particles was also confirmed in the analysis where a significant reduction along L_{002} ratio was seen in case of T20 compared to diesel. As for the medium load testing, a similar trend to the low load condition was observed for L_{002} and T_f. However, the post-SCR particles presented slightly shorter d_{002}, highlighting the presence of more graphitised aggregates. The combination of the thermal effect of the H_2 gas along with the increased soot-NO_2 oxidation at this relatively higher exhaust temperature (300 °C) might thermally reshape the neighbouring carbon layers in a manner that the final soot structure is slightly more graphitised [55]. However, this does not imply that the particles surviving the catalytic reactions possess a lower oxidative reactivity compared to the pre-SCR particles, since the fringes curvature have been increased by 4% while d_{002} only drops by 1%. It has been shown earlier in our previous work [40] that particle graphitisation order has a minor effect on particulate reactivity, while fringe curvature is the most influential parameter.

Following the findings of Song et al., it is believed that throughout the initial 40% of the soot burn off phase, the particles are likely to oxidise from the outside-in through a surface burning mode [56]. During the initial 20% burn off phase, the process is considered slow and the primary particle's structural variation will be basically shown along the fringe length (i.e. shorter layers), while no more than 3% variation is expected along the particle's graphitisation order. To further assess the extent to which the catalyst has oxidised the soot particles, the relationship provided by Song et al. [56] (Eq. (5)) that links the variation in dp_0 and the particles burn-off rate was applied in our analysis, assuming that the soot aggregates undergo a surface burning oxidation within the catalyst.

$$dp0\ post\ SCR / dp0\ pre\ SCR = (1+x)^{1/3} \quad (5)$$

Where x is the burn off rate.

Imputing the results reported earlier in Sections 3.4.1 and 3.4.2 regarding the differences spotted in dp_0 throughout the catalyst into Eq. (5), it can be concluded that:

the catalyst helped in oxidising the diesel and T20 particles by 8 and 10% respectively under low load condition. Thus, the nanostructural alterations recorded in this section (shorter L_{002} with minimal variation in d_{002}) fall in line with the findings of ref. [56] and further confirm that the soot particles undergoes oxidation reactions within the catalyst.

As for the higher load condition, the greater drop in dp_0 highlights that there was on average a 15% particle oxidation in the SCR process.

4. Conclusion

The impact of an Ag/Al_2O_3 catalyst on the morphology and nanostructure of the particulates and NOx emissions is dependent on fuels physical properties, in-cylinder fuel post injection (FPI) strategies and Hydrogen availability in the exhaust.

Fuel post injection can significantly modify the soot nanostructure ordering, in a manner that less graphitic particles are produced compared to the passive mode (no FPI). It is speculated that the combustion of the post fuel helped in enhancing the oxidation of the particles resulted from the main-injection phase, along with producing some additional soot (less mature compared to the passive mode) into the combustion chamber.

Particulate aggregation throughout the Ag/Al_2O_3 catalyst channels was considered as the main mechanism in the absence of the H_2 independently of the engine load. However, introducing H_2 (500 ppm) shows a remarkable reduction in the aggregate primary particle size (dp_0), highlighting the ability of the catalyst to enhance the soot oxidation kinetics even with limited residence time in low temperature regions. This effect was more apparent when increasing the engine load, thus also the exhaust temperature, where a soot burn-off extent of 15% was calculated for the medium load condition compared to 8% for the low load testing (diesel case). Combustion of the oxygenated blend (T20) improved the catalyst oxidation effect to 10% for the low load while no statistically significant number of soot particles (mostly hydrocarbon droplets) was observed for the medium load condition.

As for the catalyst de-NOx activity, FPI proved itself as a feasible replacement for the exhaust fuel injection strategy, where different HC:NOx ratios in the range of 1:1 to 4.5:1 were achieved for the low and medium load conditions. However, FPI alone was not able to significantly enhance the low temperature NOx conversion more than 25%, with small H_2 injections (500 ppm) required to improve the catalyst activity.

Acknowledgments

Innovate UK (The Technology Strategy Board, TSB) and EPSRC are acknowledged for supporting this work with the projects CREO ref 400176/149 and FACE (EP/P03117X/1), respectively. F.J. Martos expresses thanks to the government of Spain for supporting his research stay with reference PRX15/00256 at University of Birmingham. The authors would like to thank Johnson Matthey for providing the catalyst used in this work. With thanks to Advantage West Midlands and the European Regional Development Fund, funders of the Science City Research Alliance Energy Efficiency project – a collaboration between the Universities of Birmingham and Warwick.

References

[1] Y. Gao, et al., Aggregation and redispersion of silver species on alumina and sulphated alumina supports for soot oxidation, Catal. Sci. Technol. 7 (2017) 3524–3530, https://doi.org/10.1039/c7cy00831g.
[2] K. Villani, R. Brosius, J. Martens, Catalytic carbon oxidation over Ag/Al2O3, J. Catal. 236 (2005) 172–175, https://doi.org/10.1016/j.jcat.2005.09.018.
[3] G. Corro, et al., Effect of Ag, Cu, and Au incorporation on the diesel soot oxidation behavior of SiO2: role of metallic Ag, Top. Catal. 56 (2013) 467–472, https://doi.org/10.1007/s11244-013-9998-0.
[4] K. Shimizu, H. Kawachi, A. Satsuma, Study of active sites and mechanism for soot oxidation by silver-loaded ceria catalyst, Appl. Catal. B-Environ. 96 (2010) 169–175, https://doi.org/10.1016/j.apcatb.2010.02.016.
[5] E. Aneggi, et al., Soot combustion over silver-supported catalysts, Appl. Catal. B-Environ. 91 (2009) 489–498, https://doi.org/10.1016/j.apcatb.2009.06.019.
[6] Y. Yu, et al., Mechanism of the selective catalytic reduction of NOx by C2H5OH over Ag/Al2O3, Appl. Catal. B-Environ. 49 (2004) 159–171, https://doi.org/10.1016/j.apcatb.2003.12.004.
[7] K. Shimizu, A. Satsuma, Selective catalytic reduction of NO over supported silver catalysts-practical and mechanistic aspects, Phys. Chem. Chem. Phys. 8 (2006) 2677–2695, https://doi.org/10.1039/b601794k.
[8] K.-i. Shimizu, et al., Silver-alumina catalysts for selective reduction of NO by higher hydrocarbons: structure of active sites and reaction mechanism, Appl. Catal. B-Environ. 30 (2001) 151–162, https://doi.org/10.1016/S0926-3373(00)00229-0.
[9] A. Martınez-Arias, et al., Study of the lean NOx reduction with C3H6 in the presence of water over silver/alumina catalysts prepared from inverse microemulsions, Appl. Catal. B-Environ. 28 (2000) 29–41, https://doi.org/10.1016/S0926-3373(00)00160-0.
[10] K. Masuda, et al., Silver-promoted catalyst for removal of nitrogen oxides from emission of diesel engines, Appl. Catal. B-Environ. 8 (1996) 33–40, https://doi.org/10.1016/0926-3373(95)00051-8.
[11] T. Mryadera, Alumina-supported silver catalysts for the selective reduction of nitric oxide with propene and oxygen-containing organic compounds, Appl. Catal. B-Environ. 2 (1993) 199–205, https://doi.org/10.1016/0926-3373(93)80048-I.
[12] V. Houel, et al., Fuel effects on the activity of silver hydrocarbon-SCR catalysts, Appl. Catal. B-Environ. 73 (2007) 203–207, https://doi.org/10.1016/j.apcatb.2006.12.005.
[13] V. Houel, et al., Promoting functions of H2 in diesel-SCR over silver catalysts, Appl. Catal. B-Environ. 77 (2007) 29–34, https://doi.org/10.1016/j.apcatb.2007.07.003.
[14] K. Theinnoi, et al., Hydrogen promotion of low-temperature passive hydrocarbon-selective catalytic reduction (SCR) over a silver catalyst, Energy Fuels 22 (2008) 4109–4114, https://doi.org/10.1021/ef8004515.
[15] J. Breen, et al., A fast transient kinetic study of the effect of H2 on the selective catalytic reduction of NOx with octane using isotopically labelled 15NO, J. Catal. 246 (2007) 1–9, https://doi.org/10.1016/j.jcat.2006.11.017.
[16] P.S. Kima, et al., Effect of H2 on deNOx performance of HC-SCR over Ag/Al2O3: Morphological, chemical, and kinetic changes, J. Catal. 301 (2013) 65–76, https://doi.org/10.1016/j.jcat.2013.01.026.
[17] K. Theinnoi, et al., Fuels combustion effects on a passive mode silver/alumina HC-SCR catalyst activity in reducing NOx, Chem. Eng. J. 158 (2010) 468–473, https://doi.org/10.1016/j.cej.2010.01.021.
[18] H. Gu, K.M. Chun, S. Song, The effects of hydrogen on the efficiency of NO x reduction via hydrocarbon-selective catalytic reduction (HC-SCR) at low temperature using various reductants, Int. J. Hydrogen Energy 40 (2015) 9602–9610, https://doi.org/10.1016/j.ijhydene.2015.05.070.
[19] J.M. Herreros, et al., Enhancing selective catalytic reduction of NOx with alternative reactants/promoters, Chem. Eng. J. 252 (2014) 47–54, https://doi.org/10.1016/j.cej.2014.04.095.
[20] M. Natarajan, et al., Oxygenates Screening for Advanced Petroleum-based Diesel Fuels Part 2: the Effect of Oxygenate Blending Compounds on Exhaust Emission. SAE Technical Paper. 2001-01-3632, (2001), https://doi.org/10.4271/2001-01-3632.
[21] M.A. Fayad, et al., Manipulating modern diesel engine particulate emission characteristics through butanol fuel blending and fuel injection strategies for efficient diesel oxidation catalysts, Appl. Energy 190 (2017) 490–500, https://doi.org/10.1016/j.apenergy.2016.12.102.
[22] K. Yamamoto, et al., Influence of Diesel Post Injection Timing on HC Emissions and Catalytic Oxidation Performance. SAE Technical Paper. 2006-01-3442, (2006), https://doi.org/10.4271/2006-01-3442.
[23] M. Jeftić, et al., Combustion and Exhaust Gas Speciation Analysis of Diesel and Butanol Post Injection. SAE Technical Paper. 2015-01-0803, (2015), https://doi.org/10.4271/2015-01-0803.
[24] D.L. Hilden, J.C. Eckstrom, L.R. Wolf, The Emissions Performance of Oxygenated Diesel Fuels in a Prototype DI Diesel Engine. SAE Technical Paper. 2001-01-0650, (2001), https://doi.org/10.4271/2001-01-0650.
[25] M. Natarajan, et al., Oxygenates for Advanced Petroleum-based Diesel Fuels: Part 1. Screening and Selection Methodology for the Oxygenates. SAE Technical Paper. 2001-01-3631, (2001), https://doi.org/10.4271/2001-01-3631.
[26] Shell Chemicals, Methyl Diproxitol Specification Sheet, (2007) (Accessed 13 March, 2018, http://webcache.googleusercontent.com/search?q=cache:I72Ijn_Y6n0J:www.alchemchemical.com/products.html%3Ffile%3Dtl_files/product_documents/MSDS/shell/glycol-ether-dpm-tech-07-01-01.pdf+&cd=2&hl=en&ct=clnk&gl=uk.
[27] S. Park, et al., Development of a reduced tri-propylene glycol monomethyl ether-n-hexadecane-poly-aromatic hydrocarbon mechanism and its application for soot prediction, Int. J. Engine Res. (2016) 969–982, https://doi.org/10.1177/1468087416632367.
[28] Eric Sattler, Comparing Methods to Determine Cetane Ratings of Fuel Blends, (2009) (Accessed 13 February, 2018, http://www.dtic.mil/dtic/tr/fulltext/u2/a513172.pdf.
[29] U. Burke, W.J. Pitz, H.J. Curran, Experimental and kinetic modeling study of the shock tube ignition of a large oxygenated fuel: tri-propylene glycol mono-methyl ether, Combust. Flame 162 (2015) 2916–2927, https://doi.org/10.1016/j.combustflame.2015.03.012.
[30] P.J.M. Frijters, Fuel Composition Impact on Heavy Duty Diesel Engine Combstion & Emissions, Eindhoven University of Technology, 2012, https://doi.org/10.6100/IR735422 PhD Thesis.
[31] M. Bogarra, et al., Study of particulate matter and gaseous emissions in gasoline direct injection engine using on-board exhaust gas fuel reforming, Appl. Energy 180 (2016) 245–255, https://doi.org/10.1016/j.apenergy.2016.07.100.
[32] M. Lapuerta, R. Ballesteros, F.J. Martos, A method to determine the fractal dimension of diesel soot agglomerates, J. Colloid Interface Sci. 303 (2006) 149–158, https://doi.org/10.1016/j.jcis.2006.07.066.
[33] M. Lapuerta, F.J. Martos, G. Martin-Gonzalez, Geometrical determination of the lacunarity of agglomerates with integer fractal dimension, J. Colloid Interface Sci. 346 (2010) 23–31, https://doi.org/10.1016/j.jcis.2010.02.016.
[34] K. Yehliu, R.L. Vander Wal, A.L. Boehman, Development of an HRTEM image analysis method to quantify carbon nanostructure, Combust. Flame 158 (2011) 1837–1851, https://doi.org/10.1016/j.combustflame.2011.01.009.
[35] M. Jeftić, et al., Effects of postinjection application with late partially premixed combustion on power production and diesel exhaust gas conditioning, J. Combust. 2011 (2011) 1–9, https://doi.org/10.1155/2011/891096.
[36] Y. Ren, et al., Combustion and emissions of a DI diesel engine fuelled with diesel-oxygenate blends, Fuel 87 (2008) 2691–2697, https://doi.org/10.1016/j.fuel.2008.02.017.
[37] M. Kousoulidou, et al., Biodiesel blend effects on common-rail diesel combustion and emissions, Fuel 89 (2010) 3442–3449, https://doi.org/10.1016/j.fuel.2010.06.034.
[38] J. Lei, Y. Bi, L. Shen, Performance and emission characteristics of diesel engine fueled with ethanol-diesel blends in different altitude regions, J. Biomed. Biotechnol. 417421 (2011) 1–10, https://doi.org/10.1155/2011/417421.
[39] H. An, et al., Modeling study of oxygenated fuels on diesel combustion: effects of oxygen concentration, cetane number and C/H ratio, Energy Convers. Manage. 90 (2015) 261–271, https://doi.org/10.1016/j.enconman.2014.11.031.
[40] N. Serhan, A. Tsolakis, F.J.B. Martos, Effect of propylene glycol ether fuelling on the different physico-chemical properties of the emitted particulate matters: implications of the soot reactivity, Fuel 219 (2018) 1–11, https://doi.org/10.1016/j.fuel.2018.01.065.
[41] P. Meakin, B. Donn, G.W. Mulholland, Collisions between point masses and fractal aggregates, Langmuir 5 (1989) 510–518, https://doi.org/10.1021/la00086a038.
[42] S. Molina, et al., A Numerical Investigation on Combustion Characteristics With the Use of Post Injection in DI Diesel Engines. SAE Technical Paper. 2010-01-1260, (2010), https://doi.org/10.4271/2010-01-1260.
[43] J. Arrègle, et al., Insights on postinjection-associated soot emissions in direct injection diesel engines, Combust. Flame 154 (2008) 448–461, https://doi.org/10.1016/j.combustflame.2008.04.021.
[44] K.-i. Shimizu, et al., Reductive activation of O2 with H2-reduced silver clusters as a key step in the H2-promoted selective catalytic reduction of NO with C3H8 over Ag/Al2O3, J. Phys. Chem. C 111 (2007) 950–959, https://doi.org/10.1021/jp066147f.
[45] M. Richter, et al., The effect of hydrogen on the selective catalytic reduction of NO in excess oxygen over Ag/Al2O3, Appl. Catal. B-Environ. 51 (2004) 261–274, https://doi.org/10.1016/j.apcatb.2004.02.015.
[46] F.C. Meunier, et al., Mechanistic aspects of the selective reduction of NO by propene

over alumina and silver-alumina catalysts, J. Catal. 187 (1999) 493–505, https://doi.org/10.1006/jcat.1999.2622.
[47] R. Brosius, et al., Adsorption chemistry of NOx on Ag/Al2O3 catalyst for selective catalytic reduction of NOx using hydrocarbons, J. Catal. 231 (2005) 344–353, https://doi.org/10.1016/j.jcat.2005.01.034.
[48] K.-I. Shimizu, M. Tsuzuki, A. Satsuma, Effects of hydrogen and oxygenated hydrocarbons on the activity and SO2-tolerance of Ag/Al2O3 for selective reduction of NO, Appl. Catal. B-Environ. 71 (2007) 80–84, https://doi.org/10.1016/j.apcatb.2006.08.009.
[49] Beverly L. Smith, Lisa S. Ott, T.J. Bruno, Composition-explicit distillation curves of diesel fuel with glycol ether and glycol ester oxygenates: fuel analysis metrology to enable decreased particulate emissions, Environ. Sci. Technol. 42 (2008) 7682–7689, https://doi.org/10.1021/es800067c.
[50] S.W.T. Sitshebo, HC-SCR of NOx Emissions Over Ag-Al2O3 Catalysts Using Diesel Fuel As a Reductant, University of Birmingham, 2010 PhD Thesis.
[51] M.A. Fayad, et al., Role of alternative fuels on particulate matter (PM) characteristics and influence of the diesel oxidation catalyst, Environ. Sci. Technol. 49 (2015) 11967–11973, https://doi.org/10.1021/acs.est.5b02447.
[52] P. Ehrburger, et al., Reactivity of Soot with Nitrogen Oxides in Exhaust Stream. SAE Technical Paper. 2002-01-1683, (2002), https://doi.org/10.4271/2002-01-1683.
[53] J. Vassallo,, E. Miró, J. Petunchi, On the role of gas-phase reactions in the mechanism of the selective reduction of NOx, Appl. Catal. B-Environ. 7 (1995) 65–78, https://doi.org/10.1016/0926-3373(95)00032-1.
[54] K. Theinnoi, et al., Diesel particulate filter regeneration strategies: study of hydrogen addition on biodiesel fuelled engines, Energy Fuels 26 (2012) 1192–1201, https://doi.org/10.1021/ef201355b.
[55] Z. Ma, et al., Effects of diesel oxidation catalyst on nanostructure and reactivity of diesel soot, Energy Fuels 28 (2014) 4376–4382, https://doi.org/10.1021/ef500467a.
[56] J. Song, et al., Examination of the oxidation behavior of biodiesel soot, Combust. Flame 146 (2006) 589–604, https://doi.org/10.1016/j.combustflame.2006.06.010.